Validation of Theory Calculations with MCFM for W Mass Measurement

K. Yue[1, *]

[1] *Department of Physics, The Hong Kong University of Science and Technology, Hong Kong S.A.R., P.R.China*

(Dated: August 25, 2023)

In this study, theoretical predictions of fixed-order (FO) calculations from MCFM [**1**] are validated using Z and W bosons in leptonic decays. The differential cross section distributions generated by MCFM, a program that calculates parton-level predictions at fixed-order in QCD including resummation terms, are compared with pseudodata of the Compact Muon Solenoid (CMS) and DYTurbo [**2**] against vector boson transverse momentum p_T^V and rapidity Y^V. Our results demonstrate that the calculations from MCFM align well with the pseudodata and the calculations from DYTurbo. The choice of parton distribution functions (PDFs) of the proton results in a few percent effect on the differential cross section distribution. The validated MCFM predictions will then be employed in a reweighting procedure to achieve a precise measurement of the W boson mass.

I. INTRODUCTION

Electroweak observables are free parameters of the Standard Model (SM) and are of great interest in particle physics. One example is the W boson mass, which its measurement has been ongoing for 40 years since its discovery in 1983 [**3**]. In the SM, the W mass is exactly predicted by its relationship with other fundamental parameters, including the fine structure constant α, the Z boson mass m_Z and the Fermi constant G_F determined from the muon lifetime [**4**]. G_F is related to the measured muon lifetime τ_μ by

$$\frac{1}{\tau_\mu} = \frac{G_F^2 m_\mu^5}{192\pi^3}(1 + \Delta q) \tag{1}$$

with Δq being higher order QED corrections. At tree level expansion, the W mass is expressed as

$$m_W^2 = m_Z^2 \left[\frac{1}{2} + \sqrt{\frac{1}{4} - \frac{\alpha\pi}{\sqrt{2}G_F m_Z^2(1-\Delta r)}}\right] \tag{2}$$

where Δr represents the higher-order radiative corrections depending on the top quark mass, Higgs boson mass or even contributions from additional particles and interactions beyond the SM. The SM fit strongly constrains the W mass to be $m_W = 80358 \pm 8$MeV [**5**], which is much more precisely determined than the experimentally measured world average value $m_W = 80385 \pm 15$MeV [**6**]. It is therefore critical to reduce the experimental uncertainty in the measurement of the W boson mass to fully utilize the predictive power of the theory.

In proton-proton (pp) collisions, one possible decay mode of the W^+ boson is $W^+ \to \mu^+\nu_\mu$ (FIG. 1), while the W^- boson can decay as $W^- \to \mu^-\bar{\nu}_\mu$. This decay mode presents a challenge in experimental measurements due to the inability to directly measure the hadronic recoil. The unknown momenta of individual partons and the missing momentum of the neutrino contribute to this measurement uncertainty. By conservation of momentum, the hadronic recoil is equal to the transverse momentum p_T^W of the W boson.

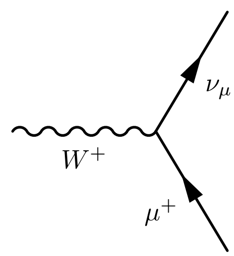

FIG. 1: Decay of a W^+ boson into an antimuon and a muon neutrino.

The dominant source of uncertainty in modeling p_T^W arises from uncertainties in PDFs, the modeling of the recoil that depends on higher-order QCD and non-perturbative effects. PDFs describe the probability distribution of partons within the proton and are phenomenological models constrained by experimental data rather than being calculable from first principle [**7**]. Our understanding of how PDFs affect various aspects of the differential cross section distribution, including boson rapidity, angular coefficients and the p_T^W distribution, is not perfect. Consequently, significant uncertainties are introduced into the analysis.

To address this issue, one approach is to employ Monte Carlo (MC) simulations of events and investigate the necessary corrections to align the simulations with data obtained from detectors. The MC simulation used to guide the measurement is created using POWHEG v2 with the MiNNLO approach [**8**][**9**], which provides this simulation with NNLO accuracy. The hadronization of partons and the decays of unstable particles were simulated using the PYTHIA 8 [**10**]. This sample was generated at leading order (LO) in quantum electrodynamics (QED), with higher-order QED effects modeled by the PHOTOS++ generator [**11**] which simulates photon radiation from the charged lepton produced in the vector boson decay. This analysis begins by validating the calculations of Z and W

* ckkyue@connect.ust.hk

decays from MCFM, which are compared against predictions from DYTurbo, as well as pseudodata of CMS. The MCFM results will then be integrated into the reweighting procedure, with the hope of achieving a more accurate W mass.

II. THEORY

A. Brief review on quantum chromodynamics

Quantum chromodynamics (QCD) is the gauge field theory that describes strong interactions and is based on the symmetry group SU(3) **[12][13]**. This symmetry produces eight gluons, which are massless gauge bosons acting as intermediate particles in strong interactions. The free parameters of QCD encompass the running coupling constant $\alpha_s(Q^2)$, which varies with the energy scale Q^2 that characterizes the interaction, and six quark masses.

The QCD Lagrangian is **[14]**

$$\mathcal{L}_{\mathrm{QCD}} = -\frac{1}{4}F^a_{\mu\nu}F^{a,\mu\nu} + \bar{\psi}^i_q(i\gamma^\mu)(D_\mu)_{ij}\psi^j_q - m_q\bar{\psi}^i_q\psi_{q,i} \tag{3}$$

where ψ^i_q denotes the quark field with colour index i, $F^a_{\mu\nu}$ with $a \in [1,8]$ is the gluon field strength tensor with colour index a, given by

$$F^a_{\mu\nu} \equiv \partial_\mu A^a_\nu - \partial_\nu A^a_\mu - g_s f^{abc} A^b_\mu A^c_\nu \tag{4}$$

and $(D_\mu)_{ij}$ is the covariant derivative

$$(D_\mu)_{ij} = \delta_{ij}\partial_\mu - ig_s t^a_{ij} A^a_\mu \tag{5}$$

A^a_μ is the gluon field with colour index a, g_s is related to the strong coupling constant α_s by $g_s^2 = 4\pi\alpha_s$ and f^{abc} are the structure constants of SU(3) such that $[t^a, t^b] = if^{abc}t^c$. t^a can be represented by the Gell-Mann matrices, which are generators of the SU(3) group, according to the equation

$$t^a = \frac{1}{2}\lambda^a \tag{6}$$

The coupling constant α_s in QCD needs to be defined at some renormalization scale μ_R, at which the subtractions to remove the ultraviolet divergences are performed. It runs logarithmically with energy according to the renormalization group equation

$$Q^2\frac{\partial\alpha_s(Q^2)}{\partial Q^2} = \frac{\partial\alpha_s(Q^2)}{\partial \ln Q^2} = \beta(\alpha_s) \tag{7}$$

where $\beta(\alpha_s)$ is the beta function and has the one-loop perturbative expansion **[12][15]**

$$\beta(\alpha_s) = -b\alpha_s^2\left[1 + \mathcal{O}(\alpha_s)\right] \tag{8}$$

where

$$b = \frac{11C_A - 2n_f}{12\pi} = \frac{33 - 2n_f}{12\pi} \tag{9}$$

Here, $C_A = 3$ is a Casimir operator, given by the trace relation $\sum_{c,d} f^{acd}f^{bcd} = C_A\delta^{ab}$. n_f is the number of active flavors.

Neglecting $\mathcal{O}(\alpha_s)$ in eq. (8), solving eq. (7) gives

$$\alpha_s(Q^2) = \frac{\alpha_s(\mu_R^2)}{1 + b\alpha_s(\mu_R^2)\ln(Q^2/\mu_R^2)} \tag{10}$$

It is sometimes convenient to define a QCD mass scale conventionally called $\Lambda \approx 200\mathrm{MeV}$ such that

$$2\alpha_s(\mu_R^2)\ln\left(\frac{\mu_R}{\Lambda}\right) \equiv 1 \tag{11}$$

and rewrite eq. (10) into

$$\alpha_s(Q^2) = \frac{1}{2b\ln(Q/\Lambda)} \tag{12}$$

Determining the value of α_s at a reference scale requires experimental fitting, and enhancing its accuracy is important in minimizing the theoretical uncertainty that affects cross section calculations for LHC processes. For instance, the value at $\mu_R = m_Z$ is the leading uncertainty in determining the total and partial hadronic Z boson widths **[16]**.

The positivity of b for $n_f \leq 16$ implies that $\alpha_s(Q^2)$ decreases with Q^2, which is the characteristic of asymptotic freedom. On the contrary, the coupling between quarks becomes strong at small Q^2, leading to quark confinement.

B. Review on PDFs

Parton distribution functions (PDFs) represent the probability density to find partons carrying a momentum fraction x at an energy scale Q. They are obtained by fits to a large number of cross section data points from numerous experiments. The evolutions of the PDFs are governed by the Altarelli-Parisi (A-P) equations **[17]**

$$\frac{d}{d\ln Q}f_g(x,Q) = \frac{\alpha_s(Q^2)}{\pi}\int_x^1 \frac{dz}{z}\Bigg\{P_{g\leftarrow q}(z)\sum_f\left[f_f\left(\frac{x}{z},Q\right) + f_{\bar{f}}\left(\frac{x}{z},Q\right)\right] + P_{g\leftarrow g}f_g\left(\frac{x}{z},Q\right)\Bigg\} \tag{13}$$

$$\frac{d}{d\ln Q}f_f(x,Q) = \frac{\alpha_s(Q^2)}{\pi}\int_x^1 \frac{dz}{z}\left[P_{q\leftarrow q}(z)f_f\left(\frac{x}{z},Q\right) + P_{q\leftarrow g}(z)f_g\left(\frac{x}{z},Q\right)\right] \tag{14}$$

$$\frac{d}{d\ln Q}f_{\bar{f}}(x,Q) = \frac{\alpha_s(Q^2)}{\pi}\int_x^1 \frac{dz}{z}\left[P_{q\leftarrow q}(z)f_{\bar{f}}\left(\frac{x}{z},Q\right)\right.$$
$$\left.+P_{q\leftarrow g}(z)f_g\left(\frac{x}{z},Q\right)\right] \tag{15}$$

$P_{g\leftarrow q}(z)$, $P_{g\leftarrow g}(z)$, $P_{q\leftarrow q}(z)$ and $P_{q\leftarrow g}(z)$ are parton splitting functions, which represent the probability of a parton splitting into two other partons. To provide an accurate description of this process, it is imperative to consider the contributions from the emission of a gluon during the transition $q \to qg$, as well as the generation of a quark-antiquark pair from a gluon via $g \to q\bar{q}$. Similarly, the gluon distribution incorporates contributions from the splittings $q \to qg$, $\bar{q} \to \bar{q}g$ and $g \to gg$.

A toy model

It is possible to construct a perturbative toy model of PDFs at small x and large Q, by applying specific approximations to the A-P equations. After solving eq. (13) and (14),

$$xf_g(x,Q) = K(Q^2)\exp\left\{\left[\frac{12}{b\pi}\omega(\xi+\xi_0)\right]^{\frac{1}{2}}\right\} \tag{16}$$

$$xf_f(x,Q) = \sqrt{\frac{\xi-\xi_0}{108b\pi\omega}}xf_g(x,Q) \tag{17}$$

where $\omega \equiv \ln\left(\frac{1}{x}\right)$ and $\xi \equiv \ln\ln\left(\frac{Q^2}{\Lambda^2}\right)$, assuming $\omega\xi \gg 1$. The derivation of eq. (16) and (17) are given in Appendix A. eq. (17) describes the distribution of sea quarks, which are flavour-independent at small x. $K(Q^2)$ represents an initial condition fitted to known properties of parton distributions, and **[18]** suggests it has the following form:

$$K(Q^2) = a_1\left[\exp(\xi-\xi_0)-a_2\right]\exp\left[-a_3(\xi-\xi_0)^{\frac{1}{2}}\right] \tag{18}$$

with $Q_0 = \sqrt{5}$GeV, $\Lambda = 200$MeV and a_i being adjustable parameters. By fitting it to one of the PDF sets used in the MCFM, specifically `NNPDF31_nnlo_as_118`, the values $[a_1, a_2, a_3] = [0.2341, 1.4409, 1.4165]$ at $Q = 100$GeV are obtained. The small x behaviors of the toy PDFs model are shown in FIG. 2.

The toy model described by eq. (16) and (17) is subsequently compared with `NNPDF31_nnlo_as_0118`, as illustrated in FIG. 3. They align well with each other as $x \to 0$, while the ratio diverges when $x \to 1$. This divergence is reasonable since the PDFs are transiting to the non-perturbative regime.

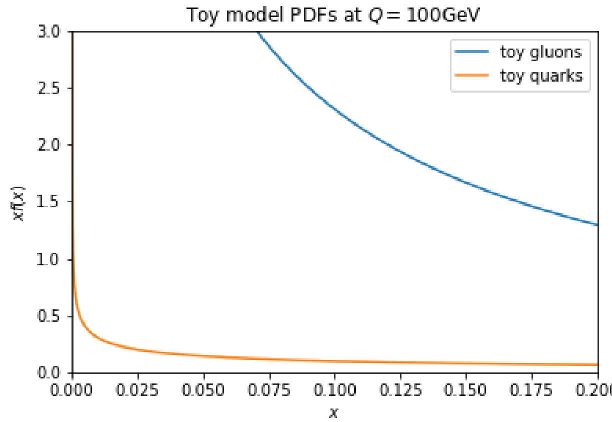

FIG. 2: Small x behaviours of the toy PDFs model. The number of active flavours is taken to be $n_f = 4$.

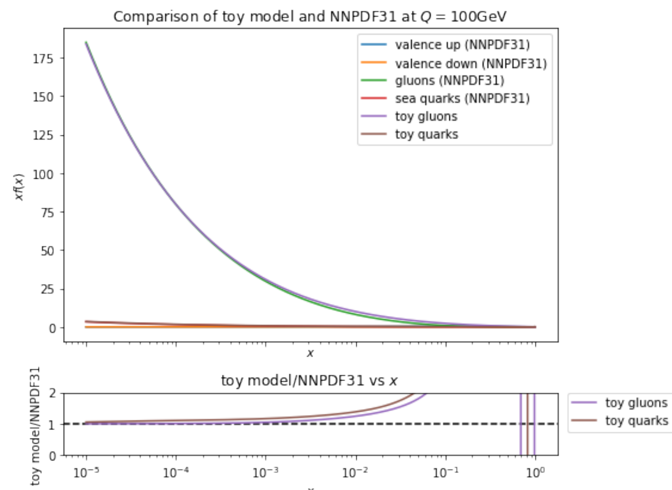

FIG. 3: Comparison between toy model and `NNPDF31_nnlo_as_0118`.

Sum rules

The quantum number of the proton is determined by its valence quarks, which are denoted as $p = uud$. Since PDFs represent the number densities of constituent partons, the following sum rules should be satisfied:

$$\int_0^1 \left[f_{u|p}(x) - f_{\bar{u}|p}(x)\right]dx = 2 \tag{19}$$

$$\int_0^1 \left[f_{d|p}(x) - f_{\bar{d}|p}(x)\right]dx = 1 \tag{20}$$

$$\int_0^1 \left[f_{q|p}(x) - f_{\bar{q}|p}(x)\right]dx = 0\,\forall q \notin \{u,d\} \tag{21}$$

Besides, the momentum sum rule states that the sum of all parton momenta should add up to the momentum of the parent hadron, which is proton in our case:

$$\sum_a \int_0^1 x_a f_{a|p}(x_a)dx_a = 1 \tag{22}$$

Let's examine if these sum rules hold for the PDF sets used in the MCFM: NNPDF31_nnlo_as_0118 and MSHT20nnlo_as118. The codes for computation were modified from [19]. The quantum numbers of the constituent partons in the PDF sets at $Q = 100\text{GeV}$ are demonstrated in TABLE I.

TABLE I: Quantum number of the constituent partons in proton at $Q = 100\text{GeV}$ for NNPDF31_nnlo_as_0118 and MSHT20nnlo_as118.

Flavour	NNPDF31	MSHT20
d	9.8937×10^{-1}	9.9138×10^{-1}
u	1.9866	1.9966
s	6.9024×10^{-3}	4.1522×10^{-3}
c	-2.5917×10^{-4}	-3.1194×10^{-4}
b	-9.2103×10^{-5}	-9.8884×10^{-5}

Both PDF sets align well with the quantum number sum rules. A similar analysis has been done to verify the momentum sum rule.

TABLE II: Momentum fraction of the constituent partons in proton at $Q = 100\text{GeV}$ for NNPDF31_nnlo_as_0118 and MSHT20nnlo_as118 (percentages presented may not sum up to exactly 100% due to rounding errors).

Flavour	NNPDF31	MSHT20
bb	1.2%	1.2%
cb	1.9%	1.9%
sb	2.8%	2.9%
ub	3.5%	3.6%
db	4.2%	4.1%
g	46.9%	46.9%
d	11.5%	11.4%
u	21.8%	21.7%
s	3.0%	3.2%
c	1.9%	1.9%
b	1.2%	1.2%
SUM	100%	100%

TABLE II reveals that gluons account for nearly half of the proton's momentum. The up quark, contributing $\sim 20\%$, represents the second largest portion, while the down quark contributes around 10%. This distribution aligns with the composition of the proton ($p = uud$). The total aggregate of the momentum fractions in both PDF sets equals to unity.

Comparison of PDF sets

The NNPDF31_nnlo_as_0118 and MSHT20nnlo_as118 PDF sets exhibit a substantial level of agreement in the central region, as depicted in FIG. 4. However, their ratios start to deviate when $x \to 1$.

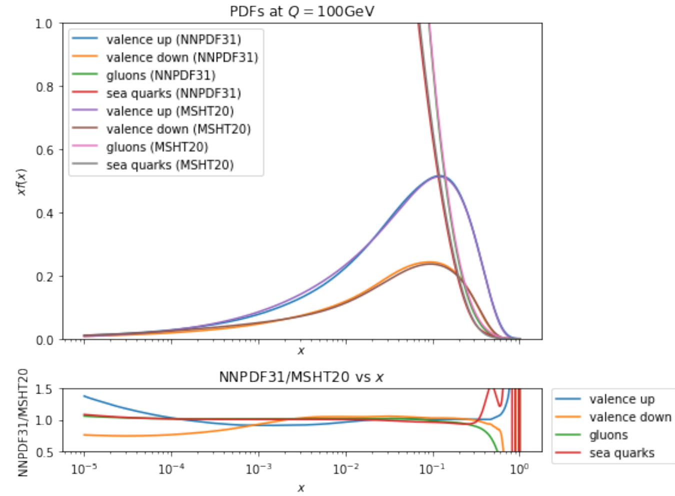

FIG. 4: Comparison between NNPDF31_nnlo_as_0118 and MSHT20nnlo_as118.

C. FO calculations and resummation

The MCFM and DYTurbo are both numerical computational programs that perform fixed-order calculations with resummation. When examining kinematic distributions at low transverse momentum q_T, the fixed-order corrections are influenced by significant Sudakov logarithms with scale ratios $\frac{Q^2}{q_T^2}$. In order to obtain reliable results from MC simulations of MiNNLO, it is necessary to enhance the fixed-order predictions by resumming these logarithms at all orders. To address this concern, MCFM combines the fixed-order colour-singlet NNLO processes [1][20][21][22].

A typical formula of cross section in perturbative QCD is

$$\sigma = \sum_{i=0}^{\infty} \alpha_s^i \sigma_i = \sigma_0 \sum_{i=0}^{\infty} \alpha_s^i \left(L^i + C^{(i)} \right) \tag{23}$$

where $L^i \sim \ln^i \left(\frac{Q^2}{q_T^2} \right)$ and $C^{(i)}$ denote the logarithm and convergent terms at the i^{th} order perturbative calculation respectively. eq. (23) can be further separated into

$$\sigma = \sigma_0 \sum_{i=0}^{n} \alpha_s^i \left(L^i + C^{(i)} \right) + \sigma_0 \sum_{i=n+1}^{\infty} \alpha_s^i L^i + \sigma_0 \sum_{i=n+1}^{\infty} C^{(i)} \tag{24}$$

The first term is the perturbative QCD (pQCD) term obtained by truncating the series at some order n, followed by the sum of higher-order logarithms, and the final term, which is convergent and hence negligible. Even if the coupling constant is small, the term $\alpha_s \ln^i \left(\frac{Q^2}{q_T^2} \right)$ can still be of the order $\mathcal{O}(1)$ when q_T is small, rendering the pQCD term inaccurate. Therefore, it becomes necessary to systematically resum the terms L^i to all orders while disregarding the constant higher-order corrections. This approach allows for obtaining a feasible prediction comparable to experimental data.

The resummed predictions consists of three contributions: (1) purely resummed contributions at small q_T, (2) fixed-order contributions at large q_T and (3) fixed-order expansion of the resummed results, which remove an overlap with the fixed-order. The MCFM provides a N^{3}LL+NNLO calculation, which corresponds to `part=resNNLO` in the configuration file. A detailed description of possible values of `part` can be found in TABLE III.

For N^{3}LL+NNLO,

$$\left.\frac{d\sigma^{\mathrm{N^3LL}}}{dq_T}\right|_{\text{matched to NNLO}} = \frac{d\sigma^{\mathrm{N^3LL}}}{dq_T} + \frac{d\sigma^{\mathrm{NNLO}}}{dq_T} - \left.\frac{d\sigma^{\mathrm{N^3LL}}}{dq_T}\right|_{\text{exp. to NNLO}} \tag{25}$$

where the last two term is defined to be the matching correction $\Delta\sigma \equiv \frac{d\sigma^{\mathrm{NNLO}}}{dq_T} - \left.\frac{d\sigma^{\mathrm{N^3LL}}}{dq_T}\right|_{\text{exp. to NNLO}}$.

Such resummation leads to two problems in practice [**23**]. Firstly, the resummed result is based on the $q_T \to 0$ limit, which may induce unphysical behavior at large q_T. Another issue is that numerically, the cancellation is imperfect, causing the matched result at very small q_T to suffer from large numerical noise. To resolve these two issues, the matching correction is switched off at very low q_T, below a cutoff scale $q_T < q_0 \lesssim 1\mathrm{GeV}$. The resummation is also switched off at large q_T using a transition function.

The transition function $t(x)$ is chosen such that

$$t(x) = \begin{cases} 1 + \mathcal{O}(x), x \to 0 \\ 0, x \geq 1 \end{cases} \tag{26}$$

where $x \equiv \frac{q_T^2}{Q^2}$. This modifies eq. (25) into

$$\left.\frac{d\sigma^{\mathrm{N^3LL}}}{dq_T}\right|_{\text{matched to NNLO}} = t(x)\left(\frac{d\sigma^{\mathrm{N^3LL}}}{dq_T} + \Delta\sigma|_{q_T>q_0}\right) + [1-t(x)]\,\frac{d\sigma^{\mathrm{NNLO}}}{dq_T} \tag{27}$$

More details of the transition function are provided in Appendix B.

D. CMS experiment

The CMS is a multipurpose detector located at the Large Hadron Collider (LHC). By observing *pp* collisions, its prime motivation is to study the SM, including the Higgs mechanism, search for new physics beyond the SM and particles that could make up dark matter. Along with the A Toroidal LHC Apparatus (ATLAS) experiment, CMS is well-known for the discovery of Higgs boson in 2012 [**24**][**25**].

The CMS detector has overall dimensions of 21.6m in length, 14.6m in diameter and a total weight of 12500t [**26**]. As demonstrated by the layout [**27**] of CMS (FIG. 5), it is built around a 4T superconducting solenoid [**28**], which provides a large bending power of 12Tm before the muon bending angle is measured by the muon system.

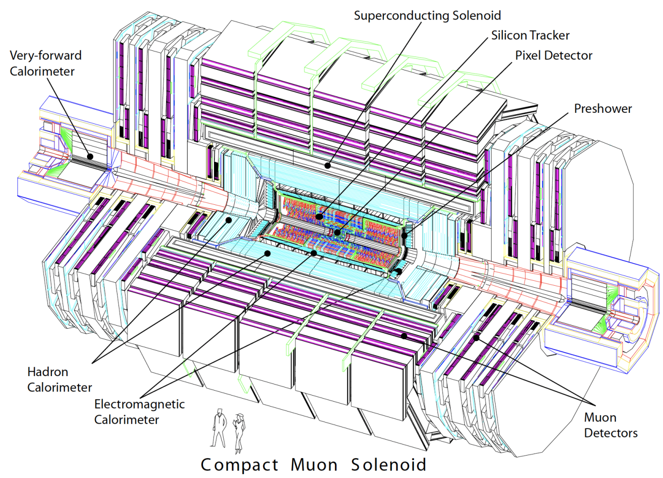

FIG. 5: A perspective view of the CMS detector [**26**].

The inner tracking system of the CMS detector is carefully engineered to offer a precise and efficient measurement of the trajectories of charged particles that emerge from the collisions at LHC, as well as to achieve accurate reconstructions of secondary vertices. It employs silicon strip and pixel detectors positioned in close proximity to the collision point, enabling reliable particle tracking. The tracker relies on the detection of small electrical signals emitted by the silicon material upon ionization caused by charged particles produced from collisions. Afterwards, these ionized charges are detected and converted into electronic signals.

The second layer is the electromagnetic calorimeter (ECAL), which makes use of scintillating lead tungstate ($PbWO_4$) crystals to measure the energy of electrons and photons generated in the collision. The choice of $PbWO_4$ crystals is justified for LHC operations due to their specific characteristics [**29**]. With a high density of 8.28gcm^{-3}, a short radiation length of 0.89cm and a small Molière radius of 2.2cm, these crystals enable the construction of a compact calorimeter with fine resolution. When high-energy electrons and photons interact with the $PbWO_4$ crystals, they produce a shower of secondary particles that release energy within the crystals, generating scintillation detectable by photodetectors. The ECAL determines the energy of incident particles precisely by measuring the light intensity.

The Hadronic Calorimeter (HCAL) is situated after the ECAL and is important for measuring hadron jets, non-interacting particles like neutrinos that lead to missing transverse momentum [**27**]. Surrounding the ECAL, the HCAL is constructed using alternating layers of brass and steel as absorbers. Additionally, it consists of approximately 70000 plastic scintillator tiles as the active material. When a high-energy hadron passes through the HCAL, it initiates a cascade of secondary particles due to nuclear interactions with the absorber material. These secondary particles deposit their energy in the scintillator tiles, producing light which is then converted by wavelength-shifting (WLS) fibres embedded in the scintillator tiles and directed to hybrid photodiodes (HPDs) through fibres. The HPDs act as photodetectors that provide gain and operate in high axial magnetic fields.

The fourth layer is a massive superconducting NbTi solenoid [**30**] enclosed in a 12000t steel return yoke. The magnet was designed to reach a 4T field within a free bore diameter of 6m and length of 12.5m, capable of storing up to 2.6 GJ of energy at full current [**31**][**32**]. A detailed map of the magnetic field is required for accurate simulation and reconstruction of physics events in the CMS detector. Using a large dataset of cosmic muons detected, the field strength within the steel barrel yoke was measured with a precision ranging from 3 to 8% depending on location [**33**]. This magnetic field enables the precise measurement of momentum and charge of charged particles passing through the tracker by analyzing their curved trajectories.

The final layer of the muon system is dedicated to muon detection, which is essential for identifying significant processes amidst the high background rate expected at the LHC. One such process is the decay of the Higgs boson into two Z bosons which then decay into four leptons. Achieving the best particle mass resolution requires all leptons to be muons, as they are less affected by radiative losses in the tracker material compared to electrons. The muon system consists of three types of gaseous detectors: in total, there are 250 drift tubes, 540 cathode strip chambers and 610 resistive plate chambers [**34**]. Drift tubes are applied for precise trajectory measurements in the central barrel region, while cathode strip chambers are used in the end caps. Resistive plate chambers provide a rapid signal upon muon passage through the muon detector and are installed in both the barrel and the end caps.

III. METHODS

Throughout this project, the theoretical calculations of the differential cross section distributions of $Z \to \mu\mu$ from two versions of MCFM, namely 10.2.2 and 10.3, are compared with pseudodata obtained from CMS and predictions from DYTurbo. For DYTurbo, comparisons using $W^+ \to \mu^+\nu_\mu$ and $W^- \to \mu^-\bar{\nu}_\mu$ are also included. Two different PDF sets, `NNPDF31_nnlo_as_0118` and `MSHT20nnlo_as118` [**35**] have been used.

The input configurations of the MCFM calculations are controlled by modifying the files `input_Z.ini` and `input_W.ini`. Additionally, modifications are made to the binning of the produced histograms using `nplotter_Z_new.f90` and `nplotter_W_new.f90`. Different parameters of `part`, which determine the accuracy in performing the MCFM calculations, have been selected. The available options for the `part` parameter are shown in TABLE III. MCFM 10.3 introduces jet-veto resummation for color singlet final states, achieving partial N^{3}LL accuracy, denoted as N^{3}LLp.

TABLE III: Possible selections of the parameter `part` that correspond to performing a calculation including large-log resummation [**1**][**20**].

`part`	description
`LO`	NLL resummed and matched
`resonlyNNLO`	N^{3}LL resummed only
`resNLO`	NNLL resummed, matched to NLO
`resNLOp`	N^{3}LL resummed, matched to NLO
`resNNLO`	N^{3}LL resummed, matched to NNLO
`resNNLOp`	N^{3}LLp resummed, matched to NNLO
`resonlyNNLOp`	N^{3}LLp resummed only
`resonlyN3LO`	N^{4}LL resummed only

The DYTurbo uses MSHT20 PDF sets, and its calculations achieve an accuracy of N^{3}LL + NNLO. The comparison between DYTurbo and MCFM results is performed in an inclusive manner. Since Z dilepton decay involves a virtual photon, an invariant mass cut of $m_{ll} \in [60, 120]$GeV is applied to the muons, with no mass cut imposed on W decay. No electroweak correction is applied in this analysis.

Conversely, the pseudodata of the CMS was produced using an MC generator that incorporates NNLO matrix elements [**8**], i.e. the MiNNLO without resummation, which subsequently used SCETlib+DYTurbo to reweight the samples [**36**] to correct for the p_T^{ll} and Y^{ll} distributions and fit at the non-perturbative regime. PHOTOS++ is applied to simulate photon radiation from the charged lepton produced in the vector boson decay. To match the settings of the pseudodata, fiducial cuts are applied to the muon producing events. These cuts include a requirement on the lepton transverse momentum, $p_T^l \in [26, 60]$GeV, and a restriction on the pseudorapidity, $|\eta^l| < 2.4$. An invariant mass cut of $m_{ll} \in [60, 120]$GeV is also imposed on the muons. Once again, no electroweak correction is taken into account.

In both comparisons, χ^2_ν analyses have been conducted to assess the goodness of fit of the MCFM results in relation to the DYTurbo calculations and pseudodata. To compare with the pseudodata from CMS, the covariance matrices are included, neglecting the off-diagonal terms of MCFM's covariance matrix. To evaluate the agreement in the non-perturbative region, it is beneficial to compute the χ^2_ν separately for low p_T^V values ($<$ 30GeV).

IV. RESULTS

A. Inconsistency in N^{3}LLp+NNLO

Before comparing the MCFM results with DYTurbo and pseudodata from the CMS, an inconsistency is observed when selecting `part=resNNLOp` in version 10.3, which corresponds to N^{3}LLp+NNLO. The PDF set employed is `NNPDF31_nnlo_as_0118`. A lower limit of $m_{ll} > 76.1876\text{GeV}$ is imposed on the invariant mass of the leptons, and a restriction is applied to the lepton transverse momentum, $p_T^l \in [20, 60]\text{GeV}$. Other configurations remain the same as the default.

To thoroughly investigate this issue, the differential cross section distributions against p_T^Z and $|Y^Z|$ are compared with those obtained using a different `part`, involving both versions 10.2.2 and 10.3.

The N^{3}LLp+NNLO (10.3) (grey curve) shows a much higher peak than the other `part` in the p_T^Z distribution. A similar feature is observed in the $|Y^Z|$ distribution, while the normalized $|Y^Z|$ distribution does not show deviation from other `part`.

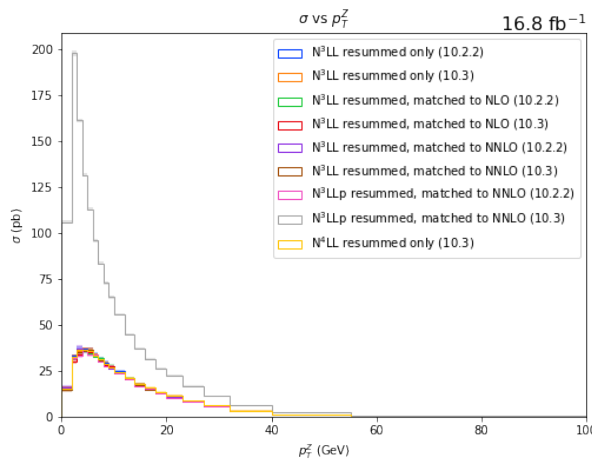

FIG. 6: Comparison of p_T^Z distributions between N^{3}LLp+NNLO (10.3) and other `part`.

After discussing with Dr. Tobias Neumann, one of the authors of MCFM, a better understanding of the reason behind the inconsistency is gained. As explained in Section C, the resummed predictions consists of three contributions: (1) purely resummed contributions at small q_T, (2) fixed-order contributions at large q_T and (3) fixed-order expansion of the resummed results.

When running MCFM, the incorporation of N^{3}LLp+NNLO introduces changes to the resummation part by including additional three-loop α_s^3 contributions. The matching correction to the fixed-order, which contains the fixed-order and the fixed-order expansion of the resummed result, should only be at the α_s^2 level. However, in MCFM 10.3, the fixed-order expansion up to α_s^3 is erroneously included.

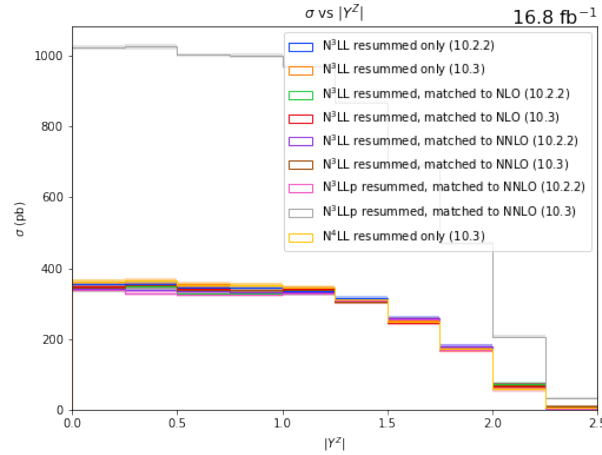

FIG. 7: Comparison of $|Y^Z|$ distributions between N^{3}LLp+NNLO (10.3) and other `part`.

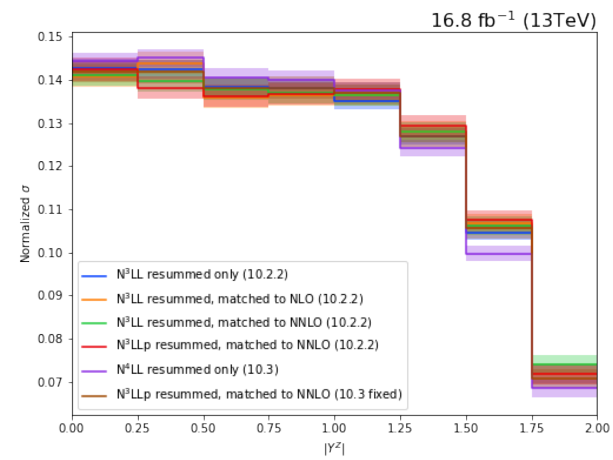

FIG. 8: Comparison of normalized $|Y^Z|$ distributions between N^{3}LLp+NNLO (10.3) and other `part`.

The bug is resolved by changing `if (order >= 7) then` to `if (order >= 8) then` at Line 1314 in `src/CuTe-MCFM/mod_Resummation.f90`, which removes the additional α_s^3 piece of the fixed-order expansion. The p_T^Z and $|Y^Z|$ distributions after fixing are demonstrated in FIG. 9 and 10, which show agreement with other `part`.

B. Resummation in N^{3}LL+NNLO

To further investigate how resummation works in MCFM, the three components of N^{3}LL+NNLO, namely the purely resummed N^{3}LL (`resonlyNNLO`), the fixed-order expansion of the resummed result to NNLO

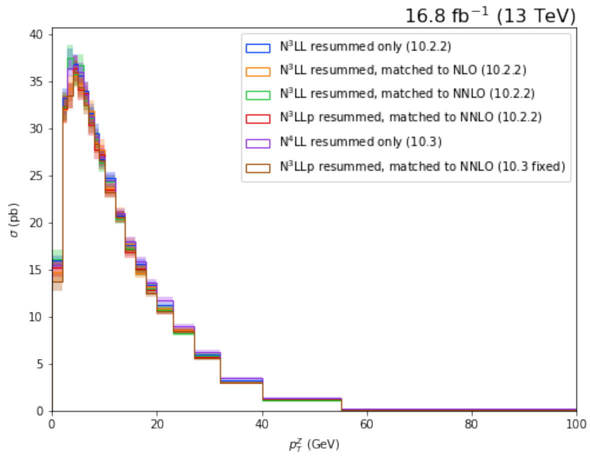

FIG. 9: Comparison of p_T^Z distributions between N^{3}LLp+NNLO (10.3 fixed) and other `part`.

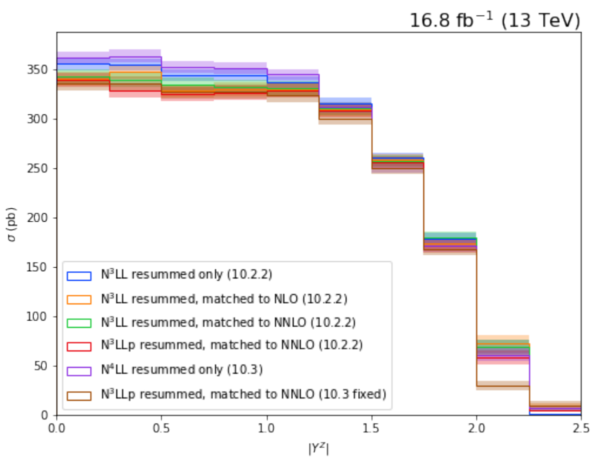

FIG. 10: Comparison of $|Y^Z|$ distributions between N^{3}LLp+NNLO (10.3 fixed) and other `part`.

(`resexpNNLO`), and the fixed-order part (`resaboveNNLO`), are plotted for $Z \to \mu\mu$ in FIG. 11 and FIG. 12. The fixed-order expansion cancels out towards the fixed-order part, as demonstrated in the p_T^Z and $|Y^Z|$ distributions.

The summation of the three separate pieces gives back the p_T^Z distribution of N^{3}LL+NNLO, as shown in FIG. 13 and FIG. 14. A sharp step is observed at 80GeV in the colour bands representing statistical uncertainties, as this is when the resummation is turned off.

C. Comparison with DYTurbo

The p_T^Z and $|Y^Z|$ distributions calculated from MCFM demonstrate a high level of consistency with predictions from DYTurbo. To ensure robustness, two distinct PDF

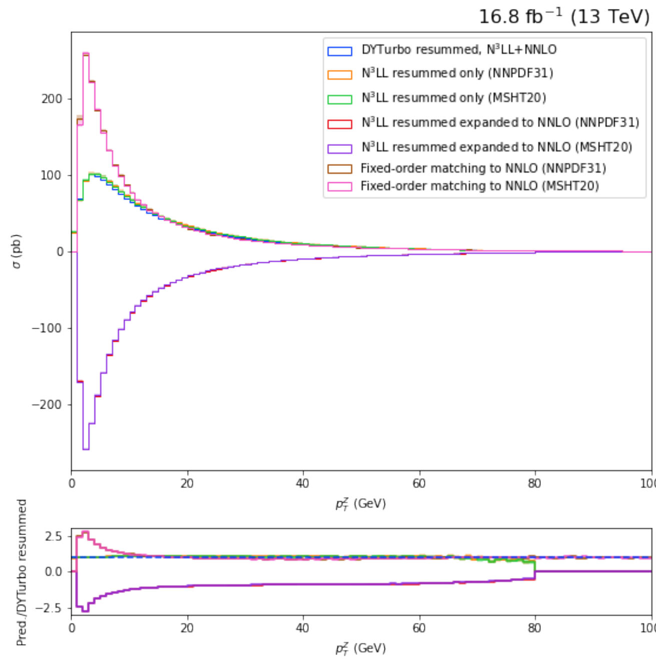

FIG. 11: p_T^Z distributions of three separate pieces in N^{3}LL+NNLO. The fixed-order expansion cancels out towards the fixed-order part.

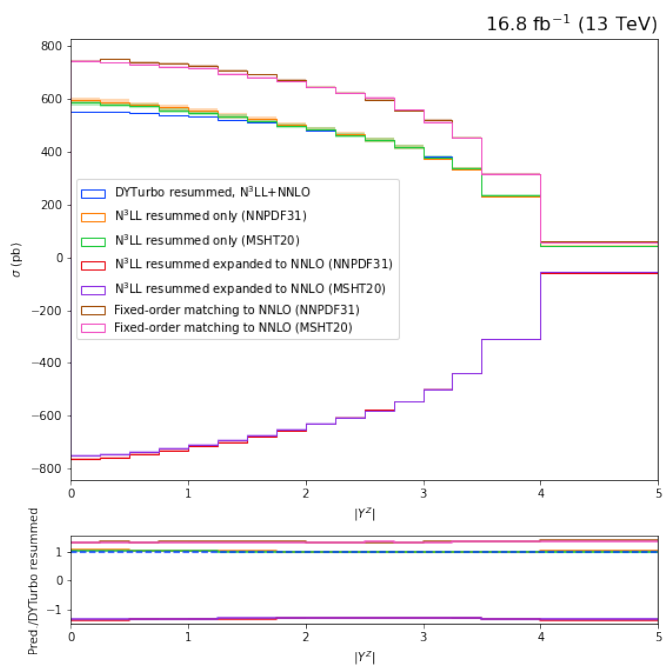

FIG. 12: $|Y^Z|$ distributions of three separate pieces in N^{3}LL+NNLO. The fixed-order expansion cancels out towards the fixed-order part.

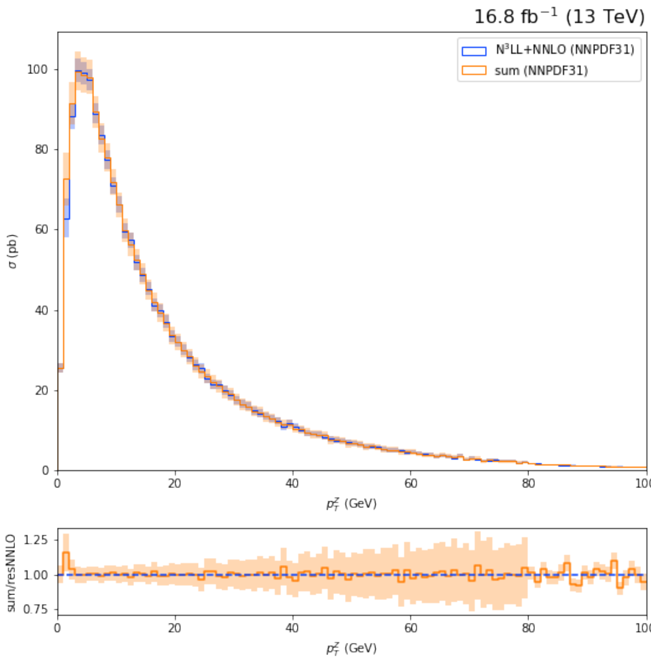

FIG. 13: Comparison of p_T^Z distributions between N^{3}LL+NNLO and the sum of three separate pieces, with the `NNPDF31_nnlo_as_0118` PDF set.

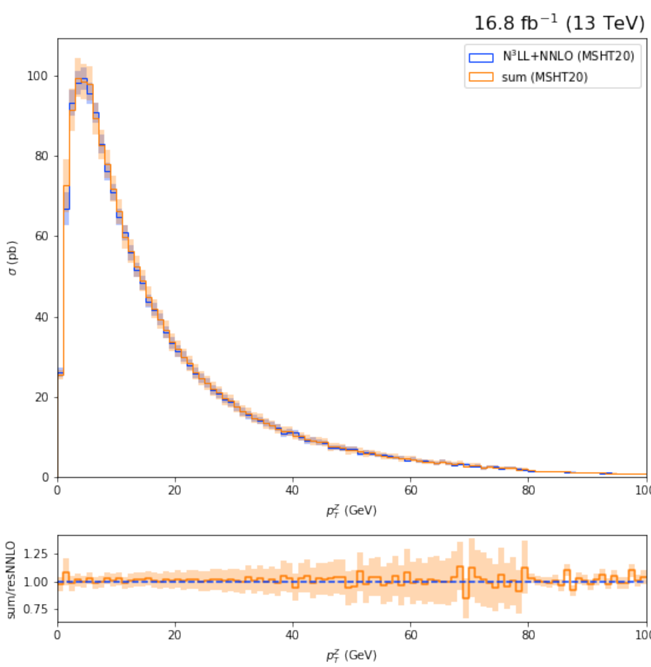

FIG. 14: Comparison of p_T^Z distributions between N^{3}LL+NNLO and the sum of three separate pieces, with the `MSHT20nnlo_as_118` PDF set.

sets, `NNPDF31_nnlo_as_0118` and `MSHT20nnlo_as118`, are applied in MCFM, and they do not exhibit any significant differences, mostly a few percent effect on the distributions. Analogous analyses are conducted for W^+ and W^-, further confirming the agreement between MCFM and DYTurbo.

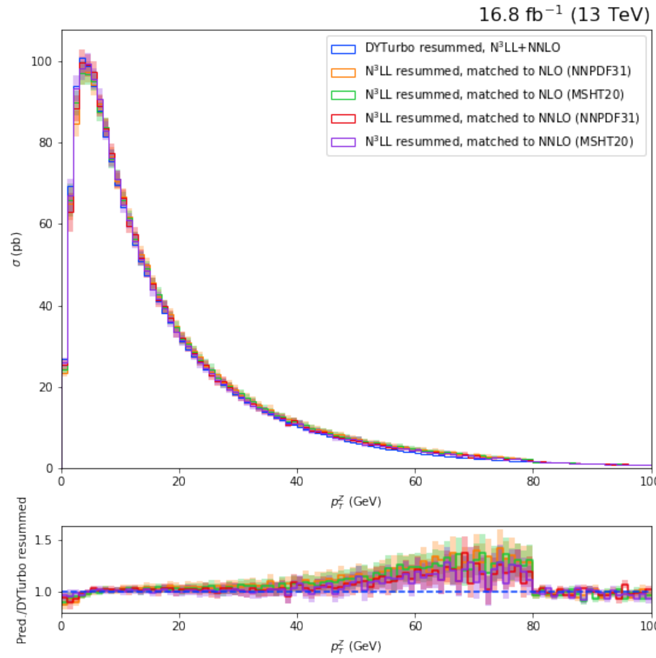

FIG. 15: Comparison of p_T^Z distributions in $Z \to \mu\mu$ between MCFM and DYTurbo using two different PDF sets.

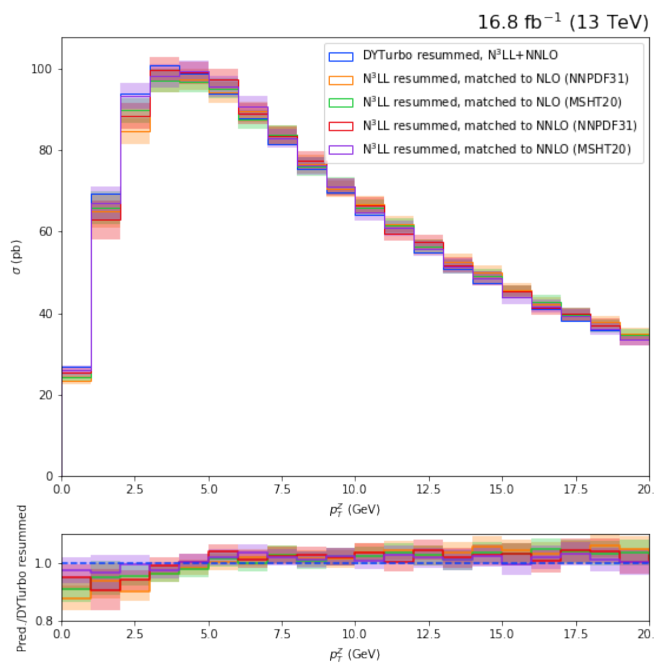

FIG. 16: Comparison of p_T^Z distributions in $Z \to \mu\mu$ between MCFM and DYTurbo using two different PDF sets in the non-perturbative region at $p_T^Z < 20$GeV.

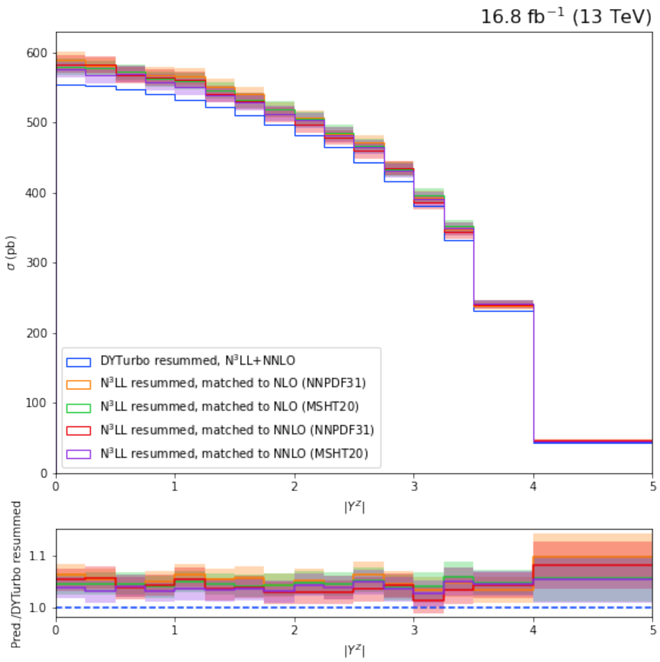

FIG. 17: Comparison of $|Y^Z|$ distributions in $Z \to \mu\mu$ between MCFM and DYTurbo using two different PDF sets.

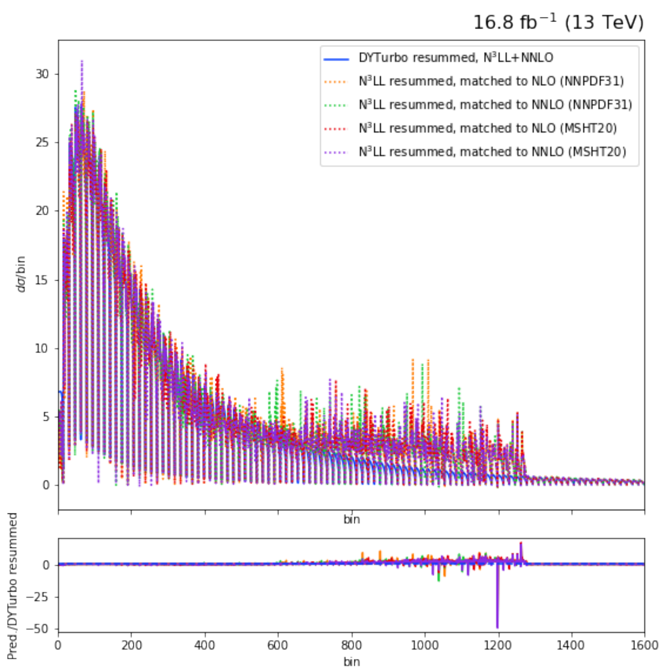

FIG. 18: Comparison of 2D bin distributions in Z decay between MCFM and DYTurbo using two different PDF sets.

Combining the p_T^V distributions in different $|Y^V|$ bin, 2D bin distributions for Z, W^+ and W^- are obtained, as illustrated by FIG. 18, 21 and 24. χ^2_ν analyses for Z, W^+ and W^- have been conducted using the 2D bin distributions, which it is assumed that the bins are uncorrelated,

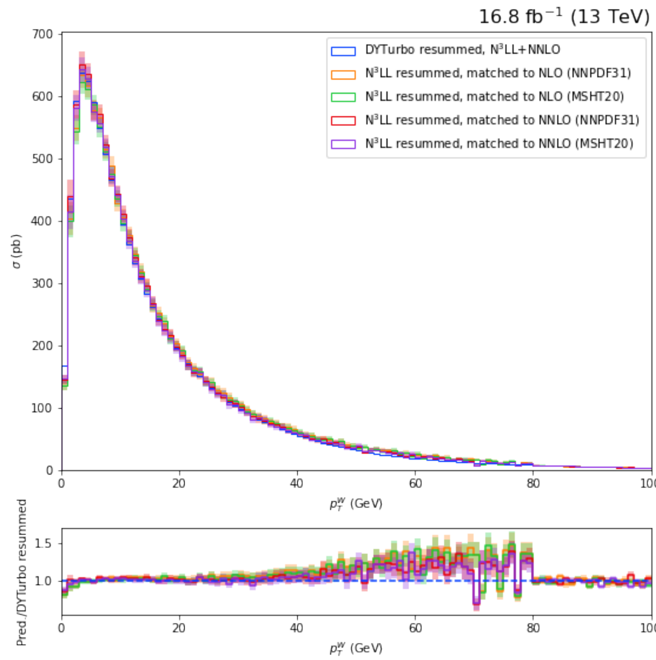

FIG. 19: Comparison of p_T^W distributions in $W^+ \to \mu^+\nu_\mu$ between MCFM and DYTurbo using two different PDF sets.

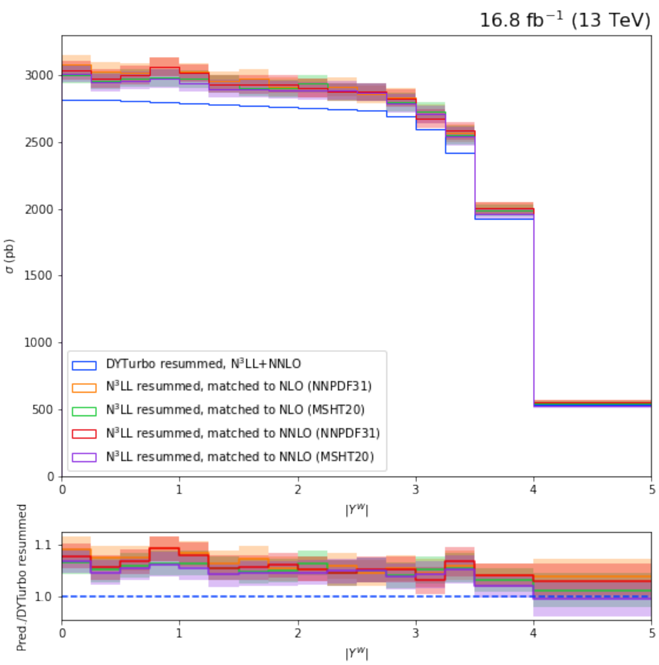

FIG. 20: Comparison of $|Y^W|$ distributions in $W^+ \to \mu^+\nu_\mu$ between MCFM and DYTurbo using two different PDF sets.

and χ^2_ν is calculated as the average of the summation of χ^2 values across all bins:

$$\chi^2_\nu = \frac{1}{N}\sum_i \frac{(v_{\mathrm{DY},i} - v_{\mathrm{MCFM},i})^2}{\sigma^2_{\mathrm{MCFM},i}} \tag{28}$$

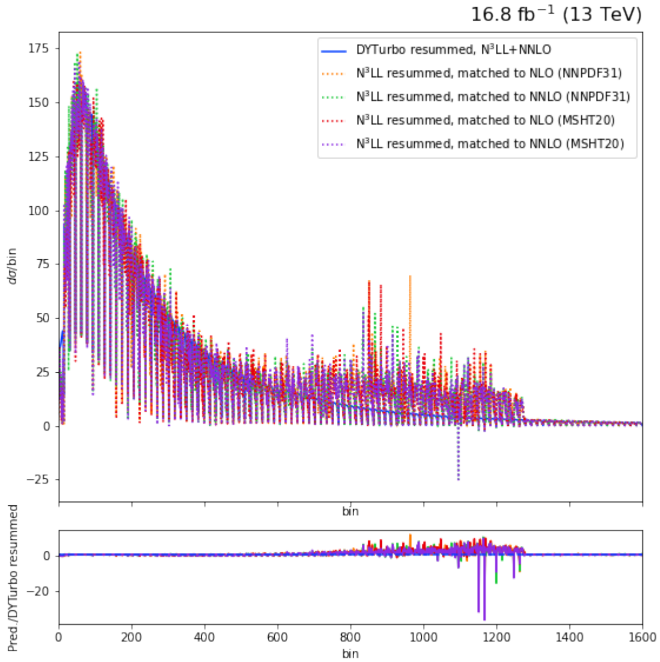

FIG. 21: Comparison of 2D bin distributions in $W^+ \to \mu^+\nu_\mu$ between MCFM and DYTurbo using two different PDF sets.

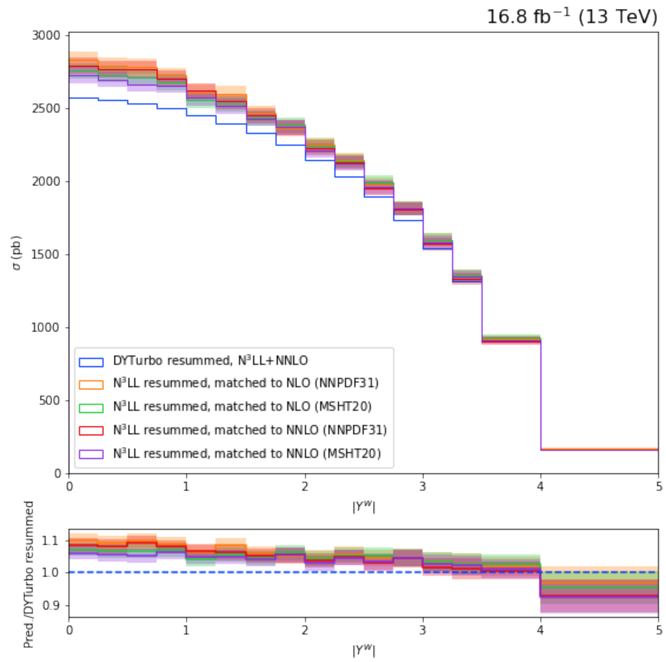

FIG. 23: Comparison of $|Y^W|$ distributions in $W^- \to \mu^-\bar{\nu}_\mu$ between MCFM and DYTurbo using two different PDF sets.

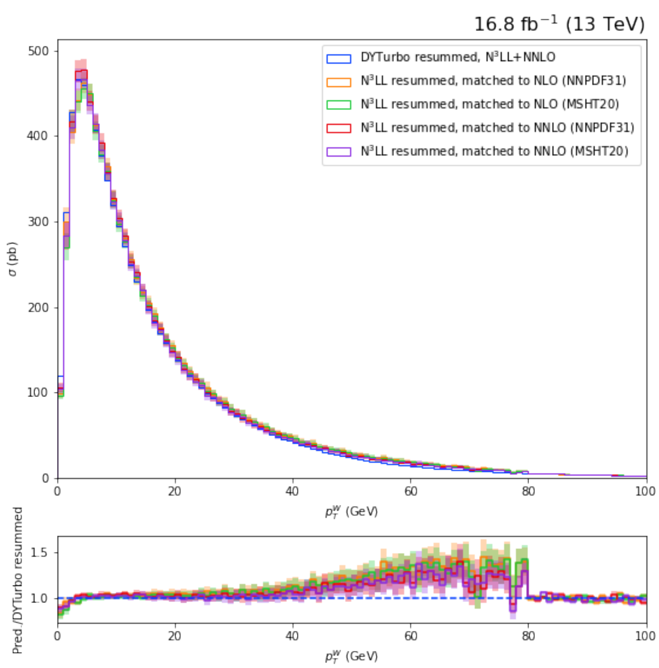

FIG. 22: Comparison of p_T^W distributions in $W^- \to \mu^-\bar{\nu}_\mu$ between MCFM and DYTurbo using two different PDF sets.

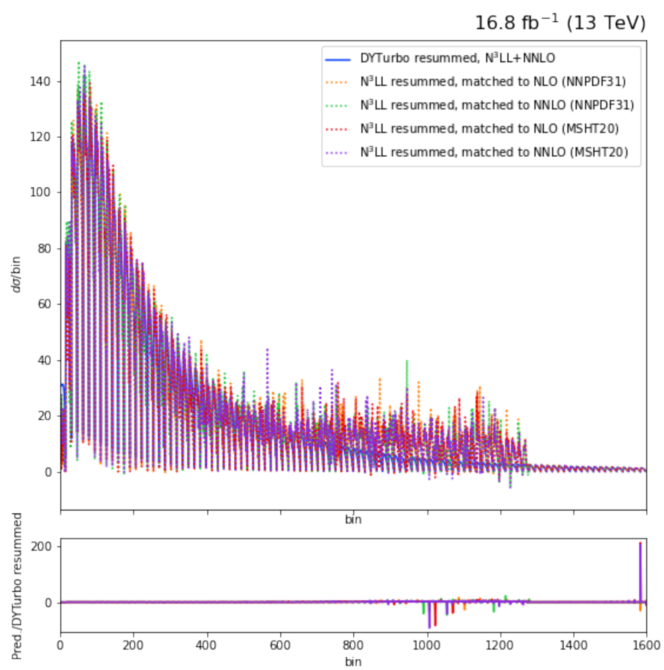

FIG. 24: Comparison of 2D bin distributions in $W^- \to \mu^-\bar{\nu}_\mu$ between MCFM and DYTurbo using two different PDF sets.

In general, the χ^2_ν value of bins with $p_T^V < 30$GeV is greater than the χ^2_ν value when considering all bins, implying a stronger discrepancy between MCFM and DYTurbo predictions in the non-perturbative regime.

TABLE IV: χ^2_ν comparison of Z, W^+ and W^- for all bins, using the `NNPDF31_nnlo_as_0118` PDF set.

	Z	W^+	W^-
N^{3}LL+NLO	4.05	5.12×10^2	9.35
N^{3}LL+NNLO	3.37	7.79	4.51

TABLE V: χ^2_ν comparison of Z, W^+ and W^- for $p_T^V < 30$GeV, using the `NNPDF31_nnlo_as_0118` PDF set.

	Z	W^+	W^-
N^{3}LL+NLO	9.00	1.70×10^3	2.61×10^1
N^{3}LL+NNLO	6.99	2.01	9.84

D. Comparison with pseudodata of the CMS

Lastly, the MCFM predictions are compared with pseudodata of the CMS for $Z \to \mu\mu$. In line with previous studies, our primary emphasis remains on analyzing the differential cross section distributions concerning p_T^Z and $|Y^Z|$.

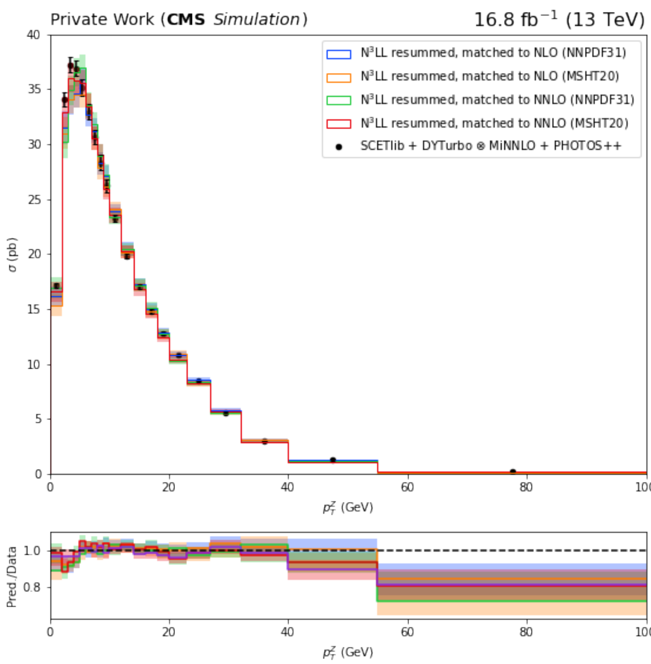

FIG. 25: Comparison of p_T^Z distributions in $Z \to \mu\mu$ between MCFM and pseudodata.

The MCFM calculations exhibit good agreement with the CMS pseudodata. In FIG. 27, a mismatch is observed in the high rapidity bin $|Y^Z| \in [2.25, 2.5]$. The pseudodata gives a value of $\sigma \approx 14.0$pb, while the MCFM prediction falls within the range of $\sigma \approx 0.6 - 1$pb. Conducting a study on the acceptance could offer further insight into this matter.

Using 2D bin distributions shown in FIG. 28, a χ^2_ν analysis taking the covariance matrices into account is performed. The diagonal elements of the MCFM bins are assigned as the variances σ_i^2, with the off-diagonal elements being disregarded. The value of χ^2_ν is given by

$$\chi^2_\nu = \frac{1}{N}\left[(\vec{v}_{\text{data}} - \vec{v}_{\text{MCFM}})^\intercal \left(\vec{K}_{\text{data}} + \vec{K}_{\text{MCFM}}\right)^{-1} (\vec{v}_{\text{data}} - \vec{v}_{\text{MCFM}})\right] \quad (29)$$

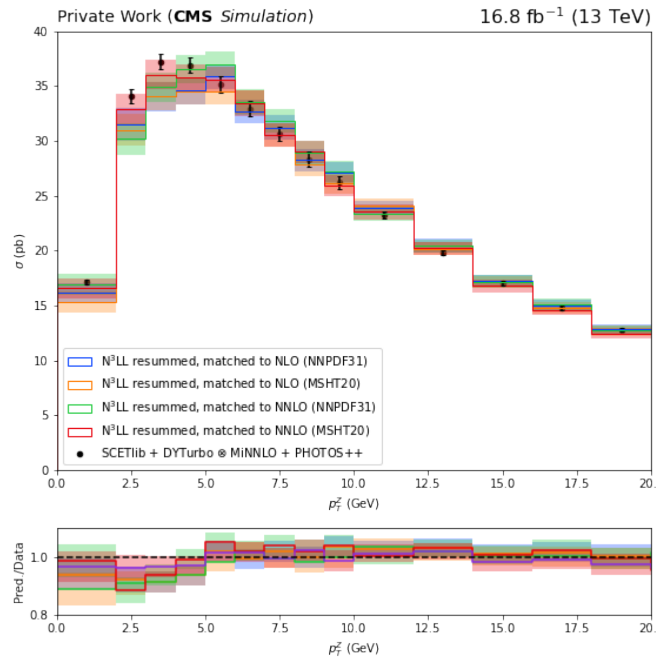

FIG. 26: Comparison of p_T^Z distributions in $Z \to \mu\mu$ between MCFM and pseudodata in the non-perturbative region at $p_T^Z < 20$GeV.

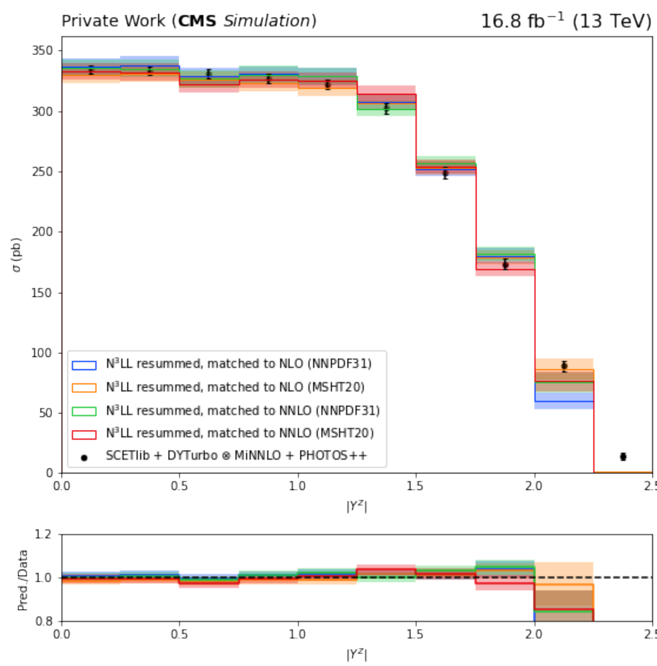

FIG. 27: Comparison of $|Y^Z|$ distributions in $Z \to \mu\mu$ between MCFM and pseudodata.

where $\vec{v}$ and $\vec{K}$ denote the values and covariance matrices respectively.

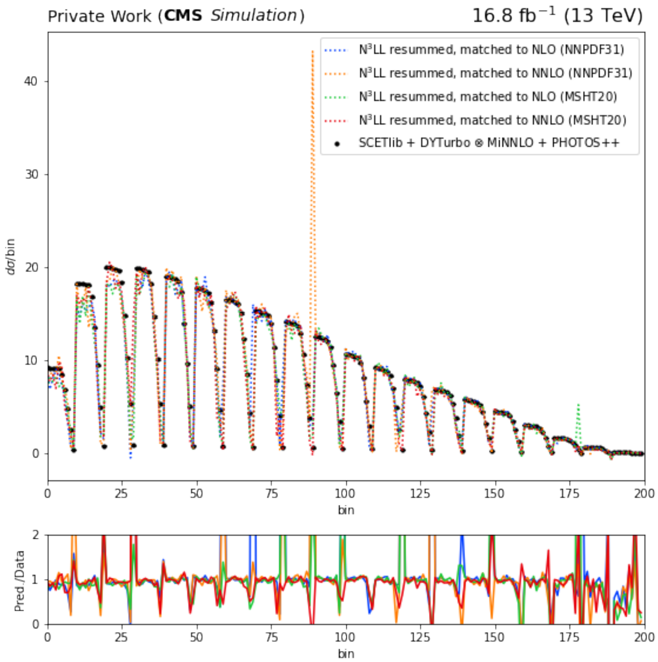

FIG. 28: Comparison of 2D bin distributions in $Z \to \mu\mu$ between MCFM and pseudodata. A strong outlier is revealed in the span $\left\{p_T^Z \in [10, 12], |Y^Z| \in [2.25, 2.5]\right\}$ bin in N^{3}LL+NNLO from the MCFM calculations, using the `NNPDF31_nnlo_as_0118` PDF set.

TABLE VI: χ^2_ν comparison of N^{3}LL+NLO and N^{3}LL+NNLO for all bins.

	NNPDF31	MSHT20
N^{3}LL+NLO	2.36	2.76
N^{3}LL+NNLO	5.46	3.72

TABLE VII: χ^2_ν comparison of N^{3}LL+NLO and N^{3}LL+NNLO for $p_T^Z < 30$GeV.

	NNPDF31	MSHT20
N^{3}LL+NLO	2.09	1.80
N^{3}LL+NNLO	3.73	2.16

V. CONCLUSION

The utilization of fixed-order numerical programs, specifically MCFM and DYTurbo, has proven instrumental in generating precise perturbative predictions through the incorporation of resummation techniques. N^{3}LL+NNLO consists of three separate pieces, which the fixed-order expansion cancels out towards the fixed-order part. Notably, the alignment between MCFM and DYTurbo predictions in the inclusive phase space demonstrates the reliability and consistency of fixed-order calculations with resummation. On top of that, fiducial results obtained from MCFM have successfully elucidated the CMS pseudodata, highlighting its accuracy in modeling experimental observations. The validated MCFM predictions can then be employed in reweighting the MC samples generated from MiNNLO.

ACKNOWLEDGMENTS

I would like to express my special thanks to my supervisors, Dr. David Walter and Dr. Pedro Silva, for the useful discussion and immense help with this research project. Additionally, I would like to extend my thanks to Dr. Tobias Neumann for his valuable advice on running the MCFM. I am also grateful to CERN for providing me with full financial support for the summer internship.

Appendix A: PDFs at small x and large Q

This section derives eq. (16) and (17). By introducing a new variable $\xi \equiv \ln\ln\left(\frac{Q^2}{\Lambda^2}\right)$, the derivative $\frac{d}{d\ln Q}$ can be expressed as $2e^{-\xi}\frac{d}{d\xi}$, and substituting it into eq. (12) gives $\alpha_s(Q^2) = \frac{e^{-\xi}}{b}$. This allows us to rewrite eq. (13) and (14) into

$$\begin{aligned}\frac{d}{d\xi}f_g(x,\xi) = \frac{1}{2b\pi}\int_x^1 \frac{dz}{z}\Bigg\{P_{g\leftarrow q}(z)\sum_f\left[f_f\left(\frac{x}{z},\xi\right)\right.\\ \left.+ f_{\bar{f}}\left(\frac{x}{z},\xi\right)\right] + P_{g\leftarrow g}f_g\left(\frac{x}{z},\xi\right)\Bigg\}\end{aligned} \tag{A1}$$

$$\begin{aligned}\frac{d}{d\xi}f_f(x,\xi) = \frac{1}{2b\pi}\int_x^1 \frac{dz}{z}\left[P_{q\leftarrow q}(z)f_f\left(\frac{x}{z},\xi\right)\right.\\ \left.+P_{q\leftarrow g}(z)f_g\left(\frac{x}{z},\xi\right)\right]\end{aligned} \tag{A2}$$

Applying two approximations: (1) gluon distribution dominates the integral in the A-P equations and (2) the function $\tilde{g}(x,Q) \equiv xf_g(x,Q)$ is slowly varying at $x \to 0$, we set $\omega \equiv \ln\left(\frac{1}{x}\right)$ and obtain

$$\begin{aligned}\frac{\partial^2}{\partial\omega\partial\xi}\tilde{g}(x,\xi) &= -x\frac{d}{dx}\left[x\frac{\partial}{\partial\xi}f_g(x,\xi)\right]\\ &\approx -x\frac{d}{dx}\left[\frac{x}{2b\pi}\int_x^1\frac{dz}{z}P_{g\leftarrow g}(z)f_g\left(\frac{x}{z},\xi\right)\right]\\ &\approx \frac{1}{2b\pi}xP_{g\leftarrow g}(x)f_g(x,\xi)\\ &\approx \frac{3}{b\pi}\tilde{g}(x,\xi)\end{aligned} \tag{A3}$$

which we have used $xP_{g\leftarrow g}(x) = 6$ when $x \to 0$. It is then straightforward to check that

$$\tilde{g}(x,\xi) = K(Q^2)\exp\left\{\left[\frac{12}{b\pi}\omega(\xi+\xi_0)\right]^{\frac{1}{2}}\right\} \tag{A4}$$

is a solution to eq. (A3). Applying similar approximations as before again: (1) gluon distribution dominates and (2) the function $\tilde{g}(x,Q) \equiv x f_g(x,Q)$ is slowly varying,

$$\begin{aligned}\frac{\partial}{\partial\xi}\tilde{f}(x,Q) &= x\frac{\partial}{\partial\xi}f_f(x,\xi)\\ &\approx \frac{x}{2b\pi}\int_x^1 \frac{dz}{z}P_{q\leftarrow g}(z)f_g\left(\frac{x}{z},\xi\right)\\ &= \frac{1}{4b\pi}\int_x^1 dz(2z^2-2z+1)\tilde{g}\left(\frac{x}{z},\xi\right)\\ &\approx \frac{1}{4b\pi}\left[\left(\frac{2}{3}z^3-z^2+z\right)\tilde{g}\left(\frac{x}{z},\xi\right)\right]_x^1\\ &\approx \frac{1}{6b\pi}\tilde{g}(x,\xi) \end{aligned} \quad (A5)$$

$P_{q\leftarrow g}(z) = \frac{1}{2}(2z^2-2z+1)$ is substituted in the above derivation. By direct computation,

$$\tilde{f}(x,\xi) = \sqrt{\frac{\xi-\xi_0}{108b\pi\omega}}K(Q^2)\exp\left\{\left[\frac{12}{b\pi}\omega(\xi-\xi_0)\right]^{\frac{1}{2}}\right\} \quad (A6)$$

is a solution to eq. (A5). This completes the proof of eq. (16) and (17) ■. The fitting parameters $[a_1,a_2,a_3]$ are then obtained by fitting to the `NNPDF31_nnlo_as_0118` PDF set using `curve_fit` imported from `scipy.optimize`.

Appendix B: Transition function $t(x)$

In the MCFM, it is first defined that [23]

$$s(x;l,r,u) \equiv \left\{1+\exp\left[\ln\left(\frac{1-u}{u}\right)\frac{x-m}{\omega}\right]\right\}^{-1} \quad (B1)$$

which $m = \frac{r+l}{2}$ and $\omega = \frac{r-l}{2}$. The transition function is then given by

$$t(x;x_{\min},x_{\max},u) = \begin{cases}1, & x < x_{\min}\\ \frac{s(x;x_{\min},x_{\max},u)}{s(x_{\min};x_{\min},x_{\max},u)}, & \text{otherwise}\end{cases} \quad (B2)$$

This ensures that only the naively matched result is used for $x < x_{\min} = \frac{q_0^2}{Q^2}$, and resummation is smoothly switched off when $x \to 1$.

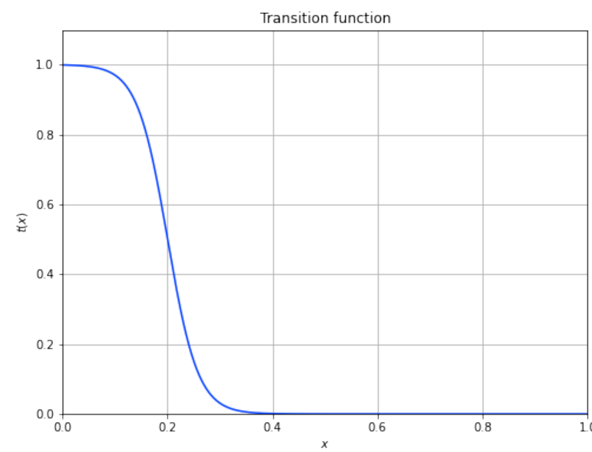

FIG. 29: The transition function $t(x)$ defined by eq. (B2), with $x_{\min} = 0.001$, $x_{\max} = 0.4$ and $u = 0.001$. Resummation is switched off for $x \geq 0.4$.

[1] J. Campbell and T. Neumann, Precision phenomenology with MCFM, Journal of High Energy Physics **2019**, 10.1007/jhep12(2019)034 (2019).

[2] S. Camarda, M. Boonekamp, G. Bozzi, *et al.*, DYTurbo: fast predictions for Drell–Yan processes, The European Physical Journal C **80**, 10.1140/epjc/s10052-020-7757-5 (2020).

[3] A. A. G. Arnison, B. Aubert, *et al.*, Experimental observation of isolated large transverse energy electrons with associated missing energy at $\sqrt{s} = 540$ GeV, Physics Letters B **122**, 103 (1983).

[4] R. G. Stuart, An Improved Determination of the Fermi Coupling Constant, G_F (1999), arXiv:hep-ph/9902257 [hep-ph].

[5] M. Baak, J. Cúth, J. Haller, *et al.* (Gfitter Group), The global electroweak fit at NNLO and prospects for the LHC and ILC, Eur. Phys. J. C **74**, 3046 (2014), arXiv:1407.3792 [hep-ph].

[6] K. A. Olive *et al.* (Particle Data Group), Review of Particle Physics, Chin. Phys. C **38**, 090001 (2014).

[7] J. Feltesse, Introduction to deep inelastic scattering: Past and present, in *20th International Workshop on Deep-Inelastic Scattering and Related Subjects* (2012) pp. 3–12.

[8] P. F. Monni, P. Nason, E. Re, M. Wiesemann, and G. Zanderighi, MiNNLO$_{\rm PS}$: a new method to match NNLO QCD to parton showers, Journal of High Energy Physics **2020**, 10.1007/jhep05(2020)143 (2020).

[9] P. F. Monni, E. Re, and M. Wiesemann, MiNNLO$_{\rm PS}$: Optimizing $2 \to 1$ hadronic processes, The European Physical Journal C **80**, 10.1140/epjc/s10052-020-08658-5 (2020).

[10] T. Sjöstrand, S. Ask, J. R. Christiansen, *et al.*, An introduction to PYTHIA 8.2, Computer Physics Communications **191**, 159 (2015).

[11] N. Davidson, T. Przedzinski, and Z. Was, PHOTOS Interface in C++; Technical and Physics Documentation (2015), arXiv:1011.0937 [hep-ph].

[12] D. J. Gross and F. Wilczek, Ultraviolet behavior of non-abelian gauge theories, Phys. Rev. Lett. **30**, 1343 (1973).

[13] H. D. Politzer, Reliable perturbative results for strong interactions?, Phys. Rev. Lett. **30**, 1346 (1973).

[14] P. Skands, QCD for Collider Physics (2012), arXiv:1104.2863 [hep-ph].

[15] W. E. Caswell, Asymptotic Behavior of Non-Abelian Gauge Theories to Two-Loop Order, Phys. Rev. Lett. **33**, 244 (1974).

[16] S. Heinemeyer, S. Jadach, and J. Reuter, Theory requirements for SM Higgs and EW precision physics at the FCC-ee (2021), arXiv:2106.11802 [hep-ph].

[17] G. Altarelli and G. Parisi, Asymptotic freedom in parton language, Nuclear Physics B **126**, 298 (1977).

[18] J. P. Ralston, POCKET PARTONOMETER, Phys. Lett. B **172**, 430 (1986).

[19] A. Huss, Parton distribution functions (2023).

[20] J. M. Campbell, R. K. Ellis, T. Neumann, and S. Seth, Jet-veto resummation at N^3LLp + NNLO in boson production processes, Journal of High Energy Physics **2023**, 10.1007/jhep04(2023)106 (2023).

[21] J. M. Campbell, R. K. Ellis, and C. Williams, Associated production of a Higgs boson at NNLO, Journal of High Energy Physics **2016**, 10.1007/jhep06(2016)179 (2016).

[22] T. Becher and M. Neubert, Drell-Yan production at small q_T, transverse parton distributions and the collinear anomaly, The European Physical Journal C **71**, 10.1140/epjc/s10052-011-1665-7 (2011).

[23] T. Becher and T. Neumann, Fiducial q_T resummation of color-singlet processes at N^3LL+NNLO, Journal of High Energy Physics **2021**, 10.1007/jhep03(2021)199 (2021).

[24] G. Aad, T. Abajyan, B. Abbott, *et al.*, Observation of a new particle in the search for the Standard Model Higgs boson with the ATLAS detector at the LHC, Physics Letters B **716**, 1 (2012).

[25] S. Chatrchyan, V. Khachatryan, A. Sirunyan, *et al.*, Observation of a new boson at a mass of 125 GeV with the CMS experiment at the LHC, Physics Letters B **716**, 30 (2012).

[26] The CMS Collaboration, S. Chatrchyan, G. Hmayakyan, V. Khachatryan, *et al.*, The CMS experiment at the CERN LHC, Journal of Instrumentation **3** (08), S08004.

[27] *Technical proposal*, LHC technical proposal (CERN, Geneva, 1994) cover title : CMS, the Compact Muon Solenoid : technical proposal.

[28] F. Kircher, P. Bredy, A. Calvo, *et al.*, Final design of the CMS solenoid cold mass, IEEE Transactions on Applied Superconductivity **10**, 407 (2000).

[29] S. Eidelman, K. Hayes, K. Olive, *et al.*, Review of Particle Physics, Physics Letters B **592**, 1 (2004), Review of Particle Physics.

[30] V. Klyukhin, Design and Description of the CMS Magnetic System Model, Symmetry **13**, 1052 (2021).

[31] A. Herve, The CMS detector magnet, IEEE Transactions on Applied Superconductivity **10**, 389 (2000).

[32] A. Herve, B. Blau, P. Bredy, *et al.*, Status of the construction of the CMS magnet, IEEE Transactions on Applied Superconductivity **14**, 542 (2004).

[33] S. Chatrchyan, V. Khachatryan, A. M. Sirunyan, *et al.* (CMS), Precise mapping of the magnetic field in the CMS barrel yoke using cosmic rays, JINST **5**, T03021, arXiv:0910.5530.

[34] J. G. Layter (CMS), *The CMS muon project: Technical Design Report*, Technical design report. CMS (CERN, Geneva, 1997).

[35] A. Buckley, J. Ferrando, S. Lloyd, K. Nordström, B. Page, M. Rüfenacht, M. Schönherr, and G. Watt, LHAPDF6: parton density access in the LHC precision era, The European Physical Journal C **75**, 10.1140/epjc/s10052-015-3318-8 (2015).

[36] M. A. Ebert and et al., SCETlib: a C++ package for numerical calculations in QCD and soft-collinear effective theory, DESY-17-099 (2018).